ADVANCED MATERIALS TECHNOLOGIES
www.advmattechnol.de

Frequency-independent Sound Absorbing Metamaterials

Semere B. Gebrekidan and Steffen Marburg*

Inspired by the concept of frequency-independent antennas in the electromagnetics, which theoretically exhibit a frequency-independent bandwidth, this paper extends the concept to acoustics by adopting a log-spiral and its modified shape to introduce a class of metamaterials called frequency-independent sound-absorbing metamaterials. Without the requirement of multiple resonators, these metamaterials achieve an ultra-broadband absorption spanning from 550 Hz for a wide range of incident angles up to 80°, using a single unit cell structure owing to Fabry–Pérot resonance, viscous boundary losses, and thermoviscous loss of the foam. Numerical and experimental analyses are provided to demonstrate the working principles of the proposed structures. Their performance is compared with archimedean spiral, and the influence of air and porous material parameters on the performance of the metamaterial is discussed in detail for normal and oblique incident waves. The underlying principle is discussed in detail, highlighting the distinctions between the proposed structures and state-of-the-art broadband metamaterials. The proposed structures represent a pioneering advancement in the field by offering compact and ultra-broadband sound-absorbing metamaterials that are suitable for practical applications.

1. Introduction

The increasing demand for noise mitigation requires the development of compact, broadband materials to expedite practical applications. Conventional approaches, such as porous materials, perforated media, acoustic blankets with mass inclusions, and gradient index materials, have commonly been employed to mitigate noise pollution.[1,2] While these approaches have shown excellent performance in the mid- and high-frequency ranges, they have failed to effectively reduce low-frequency noise due to the need for large thicknesses to dissipate the incoming noise. The concept of metamaterials (metasurfaces), originally introduced for electromagnetics,[3,4] has been extended to acoustic waves, opening up possibilities for manipulating reflected and transmitted waves, cloaking, and more.[5–11] The emergence of metamaterials has sparked a wide range of interest in the field of noise absorption by enabling near-perfect absorption in low-frequency ranges using subwavelength dimensions.[12–25] Recently, the application of metamaterials has been extended to reduce tire noise and a noise insulating chamber.[26,27] Among various metamaterial designs, space-coiling metamaterials have attracted significant attention for their ability to achieve low-frequency absorption with deep subwavelength thickness.[15,16,22–25] The extraordinary absorption performance is attributed to various mechanisms, including local resonance,[14,15] negative and zero effective material properties,[20,21] critical coupling,[16] Fabry–Pérot, and quarter-wavelength resonance.[22,23] However, despite their near-perfect absorption and deep subwavelength thickness, coiled metamaterials, and acoustic metamaterials in general, suffer from strong dispersion and narrow bandwidth due to local resonance.

To address these limitations, a common approach involves the use of multiple resonators with various resonance frequencies to broaden the bandwidth through local and nonlocal resonance mechanisms.[19,28–32] Additionally, the inclusion of porous materials within a resonant structure significantly enhances the bandwidth, while the reverse arrangement improves the low-frequency performance of porous materials by effectively trapping and slowing down sound waves.[23,33,34,37–43] By combining independent resonant absorption mechanisms, such as microperforated panels, Helmholtz resonators, and Fabry–Pérot resonators within a unit cell, broadband absorption has been achieved with relatively subwavelength dimensions.[35,44] Furthermore, theoretical derivations of effective material properties have been proposed to achieve broadband and perfect absorption for elastic waves.[36] Recently, based on the Rozanov relation,[45] originally applied to electromagnetics and relating material thickness and bandwidth, similar relations have been developed for acoustics to design optimal sound-absorbing metamaterials by employing multiple resonators.[28]

Due to the local resonance of metamaterials, most approaches employ an array of multiple resonators or a combination of various resonance mechanisms to achieve broadband absorption.

S. B. Gebrekidan, S. Marburg
Chair of Vibroacoustics of Vehicles and Machines
Technical University of Munich
85748 Garching, Germany
E-mail: semere.gebrekidan@tum.de

The ORCID identification number(s) for the author(s) of this article can be found under https://doi.org/10.1002/admt.202301239

DOI: 10.1002/admt.202301239

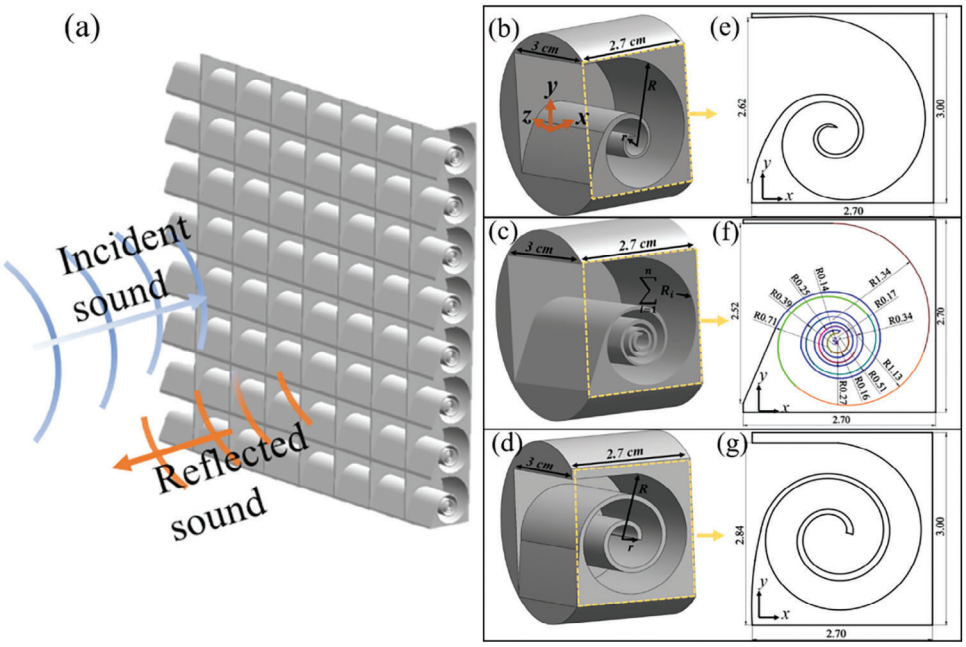

Figure 1. a) A schematic representation of incoming and reflected sound on the MLS structure. b) A 3D schematic diagram of the LS structure with a radius of $r = 1.1e^{0.2\theta}$. The outer and inner total lengths of the waveguide are 98 and 44 mm, respectively. c) The MLS structure, which is composed of different arcs and radii. The outer and inner waveguide lengths are 150 and 100 mm, respectively. d) An AS structure with the equation $r = 1 + 0.9\theta$. The outer and inner total lengths of the waveguides are 125 and 66 mm, respectively. The outer diameter of the LS, MLS, and AS structures is 40 mm. 2D representations of the e) LS, f) MLS, and g) AS structures. The 2D geometry of Figure 1e can be found in the supporting material section.[51]

The question of how to achieve performance equivalent to or exceeding that of multiple resonators using a single unit cell remains unanswered. In the field of electromagnetics, especially in radio waves, a single compact antenna known as a frequency-independent antenna has been widely implemented to enable broadband impedance matching.[45–48] These antennas possess bandwidth independent of the frequency due to their specific shapes, such as the log-spiral shape, which can be fully described in terms of angles, thus avoiding size dependence. The vanishing current at their edges allows them to exhibit theoretically frequency-independent characteristics.[47,48] However, it is important to note that the propagation of electromagnetic waves in frequency-independent antennas differs fundamentally from the propagation of sound waves in a similar structure. In the former case, propagation occurs as a result of charged particles accelerating or decelerating through the waveguide. In acoustics, log-spiral structures have mainly been employed to enhance impedance matching to increase the transmitted wave between two mediums,[49,50] and as compact quarter-wave resonators to enhance low-frequency performance in reflection problems.[24,25]

Most research focuses on achieving perfect absorption at specific low frequencies using metasurfaces or utilizing multiple coiled resonators to broaden the bandwidth. An open question remains about how to realize a compact single unit cell, without employing multiple resonators, that can achieve absorption performance comparable to or exceeding that of state-of-the-art metamaterials. Leveraging the extraordinary properties of frequency-independent antennas, we introduce a class of metamaterials called frequency-independent sound absorbers, analogous to their electromagnetic counterparts in terms of bandwidth, utilizing a single unit cell to achieve ultra-bandwidth functioning across ultra-broad incident angles. The proposed metamaterials achieve a wide-bandwidth and -angle sound absorption while maintaining an ultrathin thickness. We discuss the underlying mechanisms that lead to broadband behavior in detail, providing numerical simulations and measurements. Furthermore, we discuss the distinctions between the proposed structures and state-of-the-art sound-absorbing metamaterials, as well as clearly defined criteria for the classification of sound-absorbing metamaterials based on electromagnetic absorbers.

2. Results

2.1. Design of the Structures

3D schematic representations of the proposed structures are shown in **Figure** 1a–d. Due to their symmetric nature along the z-direction, we consider 2D cross sections, as illustrated in Figure 1e–g. The geometry of the Log-Spiral (LS) structure is defined by the equation $r(\theta) = \alpha e^{\beta\theta}$, where r and θ represent the polar coordinates, and α and β are arbitrary constants, respectively, as illustrated in Figure 1b,e. These constants determine the size and length of the structures. However, the Modified Log-Spiral structure (MLS) is composed of arcs with various radii, $\sum_1^m r_m(\theta_m)$, and the total length of such structure can be expressed by generalizing $L_e = \int_{a_i}^{b} \sqrt{r^2 + \sum_1^m (dr/d\theta)^2}\, d\theta$, where m is the number of segments, as shown in Figure 1c,f. The Archimedean Spiral (AS) is defined by $r = a + b\theta$, where a and b are

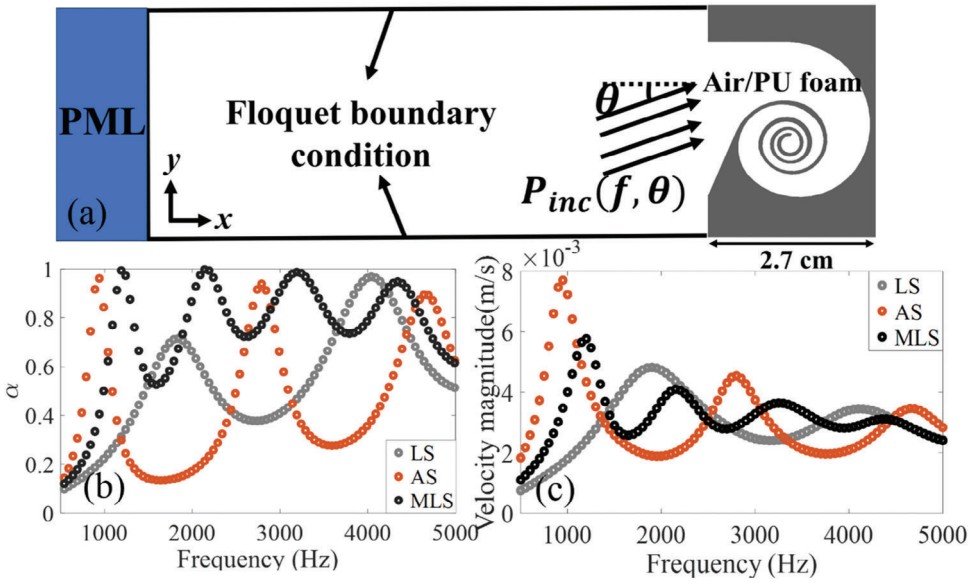

Figure 2. a) A schematic representation of a 2D simulation setting for the MLS structure under both normal and oblique incident waves. Comparison of numerical and measured absorption coefficients for b) the LS, AS, and MLS structures. c) Surface velocity magnitude for the LS, AS, and MLS structures.

constants. Consequently, the length of the spiral can be expressed as $L_e = \int_{a_i}^{b} \sqrt{r^2 + (dr/d\theta)^2}\, d\theta$, as illustrated in Figure 1d,g.

2.2. Realization of Frequency Independent Sound Absorbers

For a tapered structure with a varying cross-sectional area $S(x)$ along the path of acoustic wave propagation, the acoustic wave equation can be described in terms of 1D Webster's horn equation $\partial^2 P/\partial^2 x + (\partial \ln S(x)/\partial x)(\partial P/\partial x) = (1/c^2)(\partial^2 P/\partial^2 t)$, which exhibits a dispersion relation dependent on the geometry.[52,53] However, when the cross-sectional area remains constant, Webster's horn equation reduces to the Helmholtz equation, which can be expressed as $\nabla^2 P(r,t) = (1/c^2)\partial^2 P(r,t)/\partial t^2$, $\nabla^2 U(r,t) = (1/c^2)\partial^2 U(r,t)/\partial t^2$. These equations remain invariant under a transformation when dealing with a lossless medium with independent bulk modulus and density. Based on these equations, when the material size increases by a factor of s and the frequency reduces by a factor of $1/s$ ($x \to sx$ and $\omega \to \omega/s$), the structure's response remains similar. This invariance can be approximately maintained in materials with weak dispersion, as demonstrated in the microwave region.[54]

A theoretical acoustic analogy of frequency-independent antennas for sound absorption can be achieved by considering sound waves propagating in an infinite tapered waveguide where reflection diminishes as the velocity approaches zero. Furthermore, porous materials with a significant thickness can be used to achieve near-perfect absorption beyond the Biot frequency. However, both approaches fail to provide a realistic solution due to the substantial thickness requirement. A metamaterial composed of multiple resonators also exhibits this behavior by carefully selecting multiple overlapping resonance frequencies. Nonetheless, these methods typically require a relatively large thickness due to the need for multiple resonators. The practical limitation lies in finding a finite-sized structure capable of achieving a broad bandwidth, akin to porous layers, with subwavelength dimensions of a metamaterial resonator. In the following sections, we will demonstrate through numerical simulations and experiments that metamaterials with such properties can indeed be realized by using a unit cell spiral structure with modified geometry to enhance dissipation.

2.3. Numerical Verifications

2.3.1. Normal Incidence Absorption Performance

The absorption performances of the proposed structures have been analyzed numerically using 2D simulations in the COMSOL Multiphysics software, taking into account the thermoviscous effect and the additional loss incurred during the experiment, as depicted in **Figure** 2a. A 2D model reduces the heavy computational requirements for 3D simulations with thermoviscous effects, without sacrificing accuracy. Since the absorption mechanism primarily depends on the length of the waveguide rather than the width of the opening, 2D simulations are consistently employed throughout the paper. The numerical performance of the LS structure reveals the first and second peaks at 1900 and 4200 Hz, respectively, as demonstrated in Figure 2b, corresponding to the Fabry–Pérot resonance at $n\lambda/2$, where $n \in$ N, given an average total length of 72 mm. By shaping the LS structure with discontinuous arcs instead of a uniform parametric curve, the MLS structure achieves broadband absorption starting from 800 Hz, as shown in Figure 2b, with the absorption peaks corresponding to Fabry–Pérot resonance, given a total length of 125 mm, while the narrow features in the gradient waveguide contribute to additional loss, enhancing the absorption. However, in the case of the AS structure, with a total average length of 96 mm, the peaks appear approximately when $L_{tot} \approx n\lambda/4$, as displayed in Figure 2b. Despite the longer total

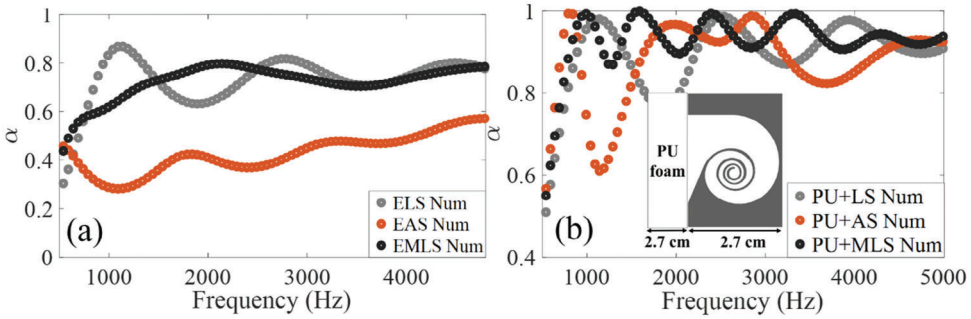

Figure 3. Absorption magnitude of a) PU foam embedded inside the LS, AS, and MLS structures, denoted as ELS, EAS, and EMLS, respectively. b). A 27 mm thick PU foam placed in front of the LS, AS, and MLS structures.

sound path in the MLS structure, the AS exhibits a lower absorption peak at 950 Hz, which contradicts the underlying physical mechanism. This discrepancy is due to the distinct absorption mechanisms of Fabry–Pérot and quarter-wavelength resonances, on which the peaks of MLS and AS structures depend. Therefore, the quarter-wave resonance ($\lambda/4$) of the AS structure yields low-frequency absorption compared to the MLS. The gradient shapes of the inlet contribute to the broadening of the bandwidth by reducing the reflected waves from the interface. As shown in Figure 2c, the magnitude of velocity at the respective resonance frequencies of LS, MLS, and AS structures is higher. The magnitude of velocity inside the MLS structure exhibits improved dips compared to the values for LS and AS, demonstrating the viscous boundary effect on absorption, irrespective of the additional loss considered during the simulation. The wavelength-to-thickness ratios (λ/D) at the first peaks for the LS, MLS, and AS structures are 6.7, 10.2, and 13.4, respectively. This indicates the subwavelength nature of the proposed structures with a degree of compactness (L_{tot}/D) of 2.67, 4.63, and 3.56, respectively.

2.3.2. Effects of Thermoviscous Loss

Two porous materials, melamine and polyurethane (PU) foam, with different flow resistivity, thermal characteristics, and viscous characteristic lengths, are considered to identify the effect of porous material parameters on absorption performance. First, we examine the effect of embedding PU foam within the LS, AS, and MLS structures, denotes as ELS, EAS, and EMLS, to understand how thermoviscous loss impacts their absorption performance. The performance of the LS structure is improved, and the first peak shifts to a lower frequency when PU foam is embedded due to thermoviscous loss and a smooth gradient path. The PU-embedded MLS structure demonstrates relatively lower performance compared to structures without PU foam, and the peaks show a lower magnitude, as illustrated in **Figure** 3a. This decrease in magnitude is attributed to the dissipation of acoustic energy by the PU foam, which, unlike the LS structure, exhibits an irregular wave path. Viscous boundary loss plays a key role in the narrow features of the wave path, in addition to a sudden change in cross-section, reducing the energy required to fully excite the Fabry–Pérot resonance modes. This effect can also be observed when PU foam is embedded in the AS structure, resulting in attenuated peaks in the low and mid-frequency ranges, as shown in Figure 3a. In this case, the viscous boundary loss has a less significant effect due to a constant cross-section of the waveguide. It is apparent that PU foam enhances the magnitude and bandwidth when embedded in a smooth gradient waveguide.

Placing PU foam in front of the LS structure shifts the resonance to a lower frequency, resulting in an improvement in absorption magnitude ($\alpha > 0.8$) across all frequencies, as illustrated in Figure 3b. Similarly, the low-frequency performance of the MLS structure improves when PU foam is placed in front of it, displaying a high absorption magnitude ($\alpha > 0.93$), as shown in Figure 3b. A similar arrangement for the AS structure yields enhanced performance, particularly in the high-frequency ranges. As depicted in Figure 3b, the low-frequency peaks remain relatively constant, despite the doubled wave propagation distance compared to the AS structure without PU foam. Additionally, an additional peak emerges at the resonance frequency of the PU foam.

2.3.3. Oblique Incident Absorption Performance

To investigate the sound-absorbing capabilities of the proposed structures at various angles of incidence, we performed numerical simulations using COMSOL Multiphysics, as depicted in Figure 2a. We applied Floquet boundary conditions along the x- and y-directions. As the angle of incidence increases, the peaks of the LS structure shift to the left and exhibit lower performance in the low-frequency range, as shown in **Figure** 4a. The second peak becomes dominant when the incidence angle exceeds 70°, while the low-frequency peak demonstrates poor performance. Near the grazing angle, a single peak emerges at 3000 Hz, which is approximately equal to the total length of the outer LS waveguide. The performance of the MLS structure improves, especially at low-frequency dips, as the angle of incidence increases, as shown in Figure 4b. When the incidence angle surpasses 60°, the peaks shift towards higher frequencies, and a noticeable dip effect becomes apparent. As the incidence angle approaches the grazing angle, we observe a low absorption performance and a consistent number of peaks with less variation in resonance frequencies, compared to the LS and AS structures. Similarly, the performance of the AS remains relatively consistent up to 60°, as shown in Figure 4c. However, as the incidence angle increases, there is a shift in resonance frequency towards higher frequency peaks at 2800 and 4800 Hz, and the magnitude of the first peak

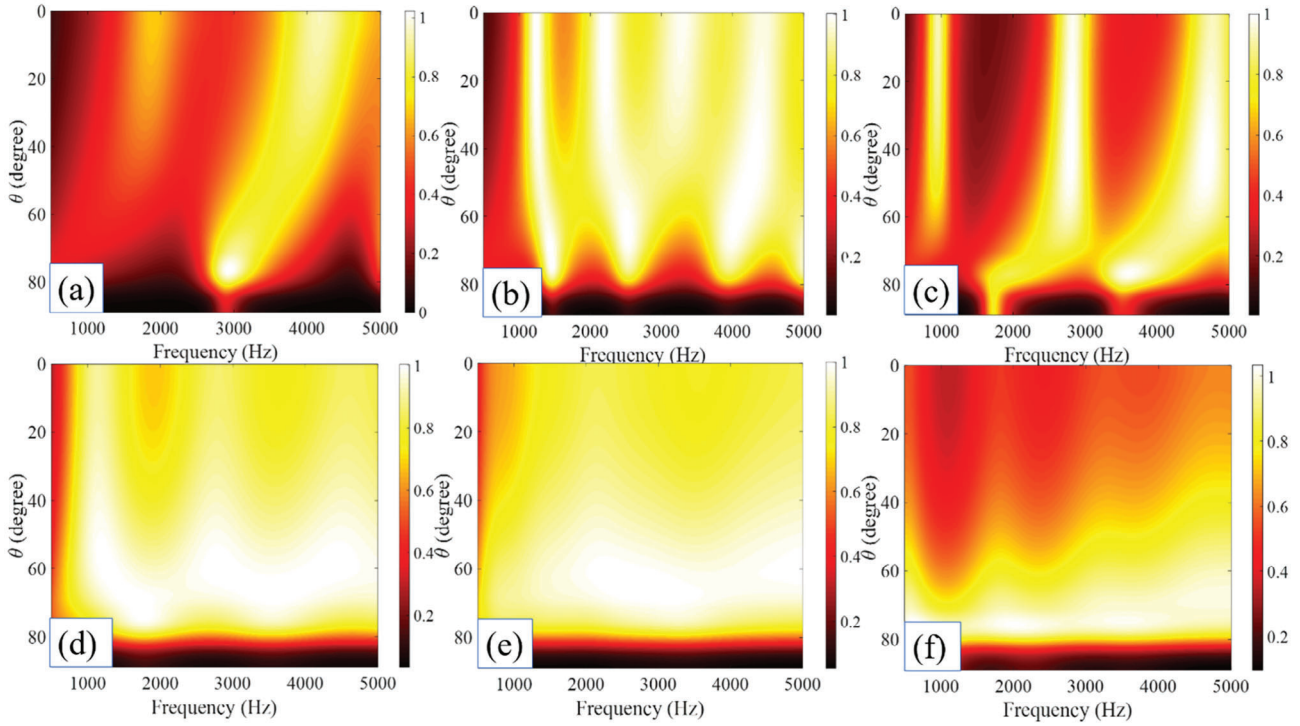

Figure 4. The absorption performance of oblique incident waves for: a) the LS structure without PU foam, b) the MLS structure without PU foam, c) the AS structure without PU foam, d) the LS structure with embedded PU foam, e) the MLS structure with embedded PU foam, and f) the AS with embedded PU foam. The dark red color corresponds to low absorption, while the bright color signifies a near unity absorption coefficient.

decreases while the high-frequency performance improves. New peaks appear at 1750 and 3500 Hz, near the grazing angle, due to resonance occurring approximately at $nc/2L$, where L represents the effective length of the AS.

Furthermore, PU foam embedded within the LS structure demonstrates superior performance when the incident angle ranges from 50° to 80°, achieving near-perfect absorption at 80°, as illustrated in Figure 4d. Moreover, when compared to both the LS structure with and without embedded foam, the resonance frequencies remain constant up to 80°, and the first and second peaks shift from 1200 to 1800 Hz and from 2800 to 3550 Hz, respectively, as depicted in Figure 4d. Similarly, the MLS structure with embedded PU foam exhibits optimal absorption between incident angles of 60° and 80°, featuring a broadband and nearly perfect absorption magnitude ($\alpha > 0.9$). It shows a moderate absorption even up to 85° before decreasing substantially near the grazing angle, as depicted in Figure 4e. Furthermore, the absorption performance of the AS improves significantly as the incident angle increases, with near-perfect absorption across the entire frequency range, as shown in Figure 4f. In comparison to the LS structure embedded with PU foam, the AS demonstrates better performance between incident angles of 70° and 80°, owing to enhanced performance at lower frequencies.

In the cases mentioned above, an increase in the incidence angle leads to multiple reflections along the boundaries. This, in combination with the thermoviscous dissipation of the foam, results in improved absorption performance and bandwidth compared to normal incident waves. Within the given frequency range, frequency-independent absorbers exhibit optimal absorption between incidence angles of 60° and 80°. Additionally, the low-frequency cutoff frequency shifts to a much lower frequency due to the longer sound propagation distance, resulting in improved dissipation compared to normal incident waves. Moderate absorption is achieved up to 85° before a significant decrease near the grazing angle. The total absorption (α_{tot}) of the proposed structures for random oblique incidence angles can be described using the Paris formula,[2]

$$\alpha_{tot} = \frac{\int_{\theta=0}^{\theta_0} \alpha(\omega, \theta) * \sin(\theta) \cos\theta d\theta}{\int_{\theta=0}^{\theta_0} \sin(\theta) \cos(\theta) d\theta} \quad (1)$$

Based on this equation, the PU embedded LS structure demonstrates improved absorption performance up to 80° and exhibits reduced overall performance when considering all incident angles, as shown in **Figure 5**a. Similarly, the MLS structure achieves an average absorption magnitude ($\alpha_{tot} > 0.8$) within incidence angles ranging from 0° to 80° across the entire frequency range. This performance is significantly higher than the overall incidence angle. Both the PU embedded LS and MLS structures show improved absorption at 80°. The AS structure shows a similar performance in both cases, indicating better performance when the incidence angle exceeds 80°, as shown in Figure 5a. The proposed structures with embedded foam show approximately similar performance across all incident angles, and they perform better compared to those without the foam arrangement. However, the PU embedded MLS structure exhibits a similar performance to that without PU foam but with improved absorption

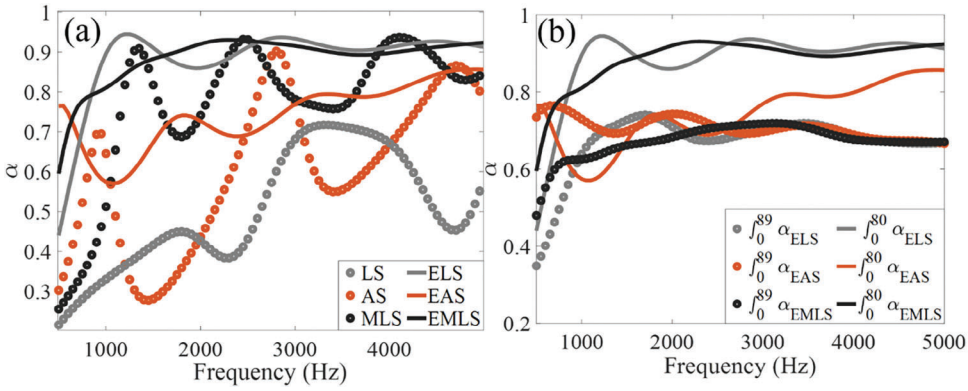

Figure 5. Absorption performance of oblique incident waves employing Paris equation for the a) LS, MLS, and AS structures, both with and without PU foam, for incidence angles ranging from 0° to 80°. b) Incorporation of PU foam within the LS (ELS), MLS (EMLS), and AS (EAS) structures for incidence angles ranging from 0° to 80° and 0° to 89°.

dips, as shown in Figure 5b. As the incident angle increases, the wave propagation distance also increases, resulting in a considerably lower cutoff frequency, a broad bandwidth, and improved performance of the MLS structure. The presence of narrow features and a gradient waveguide enhances viscous boundary loss, yielding a near-perfect absorption up to 80° incident angles. With the further inclusion of porous foams, near-flat absorption is achieved.

2.4. Experimental Verifications

To validate the numerical predictions, we conducted measurements using a standard two-microphone setup with 40 and 100 mm waveguides, as shown in **Figure 6**a,b, within the frequency intervals of 550–5000 Hz and 250–2000 Hz, respectively.[55] Since the resonance mechanisms of the AS and LS structures depend on a quarter-wavelength and Fabry–Perot resonance, respectively, the length of the waveguide has a significant influence on the observed peaks. As depicted in Figure 6f,g, the measurements obtained from the 40 mm tube align well with the resonance peaks predicted numerically for the LS and AS structures. However, the measured absorption of the MLS structure exhibits slight discrepancies compared to the numerical predictions in terms of the number of peaks and resonance frequencies, as illustrated in Figure 6h. These discrepancies are attributed to manufacturing defects affecting the submillimeter features and their resulting impact on the total sound propagation path. This dictates that not only the peaks are influenced by Fabry–Pérot resonances, but boundary viscous losses also affect the performance as a result of manufacturing errors.

Figure 7a depicts the measured absorption magnitude of embedded PU foam within the LS, AS, and MLS structures. The discrepancy between the numerical and predicted performance can be attributed to errors in the foam embedding process within the structures. Additionally, the observed variations in the measured performance of the MLS structure with embedded PU foam are primarily a result of improper fitting due to the very narrow features of the structure. Despite these variations, this configuration exhibits a limited influence on enhancing absorption performance when compared to the MLS structure without embedded foam. Simultaneously, the measured absorption of the AS structure displays trends similar to the numerical predictions, albeit with less prominent peaks, as illustrated in Figure 7a.

Replacing PU foam with melamine foam achieves similar performance, indicating the weak effect of foam characteristics, as long as the variation is not significantly large, as shown in Figure 7b. The absorption performance of the proposed structures with embedded foam yields significantly superior results compared to state-of-the-art broadband sound-absorbing metamaterials, considering the thickness-to-absorption bandwidth ratio.[28] Remarkably, the MLS structure, without melamine foam, achieves comparatively similar performance with a compact thickness compared to the periodic arrangement of resonators twice its thickness.

In **Figure 8**a, the measurement of a 27 mm PU foam with a rigid backing shows an absorption peak at 2000 Hz, which is much lower than the quarter-wavelength due to its lower flow resistivity. The performance of the PU foam placed in front of the LS structure aligns well with the numerical prediction, albeit with a shifted resonance peak, as illustrated in Figure 8a. In this arrangement, both numerical and measured magnitudes exhibit an additional peak at 2500 and 2900 Hz, respectively, owing to the thermoviscous dissipation of the foam, in comparison to when there is no PU foam. Similarly, placing PU foam in front of the MLS structure has shown a shift in resonance frequency and a nearly flat absorption profile compared to the numerical prediction, as demonstrated in Figure 8b. Additionally, the measured performance of the AS agrees well with the numerically predicted absorption, with a slight variation in magnitude observed near the resonance frequency of the PU foam, as depicted in Figure 8c. Melamine foam exhibits similar performance to the PU foam when placed in front of the proposed structures, regardless of the difference in flow resistivity, as shown in Figure 8d. The overall performances of the LS, MLS, and AS structures are improved due to the slowing of sound waves and thermoviscous dissipation in the foam. It is evident that using the proposed shapes as a rigid backing for porous materials instead of plain rigid material results in an improved low-frequency absorption.

To assess the influence of opening size on the absorption performance, we measured the absorption coefficient in the low-frequency region for the LS, MLS, and AS structures, while

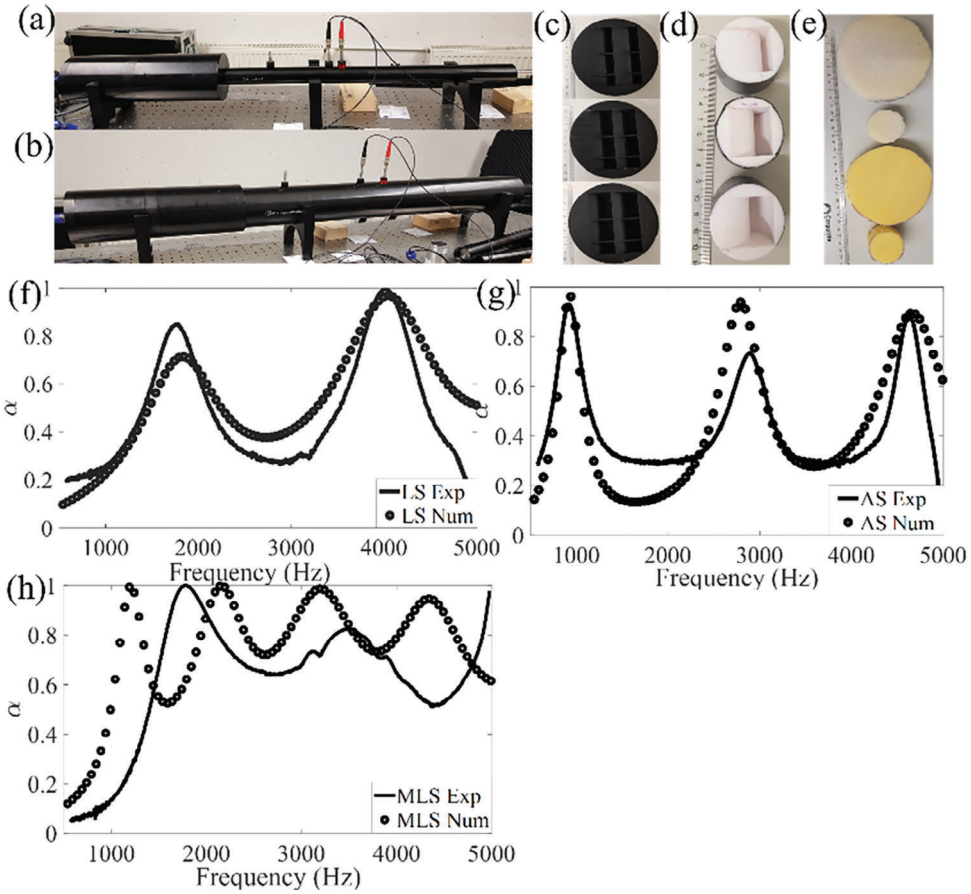

Figure 6. The experimental setup for an AED Type I two-microphone impedance tube with a) 40 mm and b) 100 mm. 3D-printed samples of structures for the AS, MLS, and LS structures, for c) low-frequency and d) high-frequency measurements. e) PU and melamine foam samples with diameters of 40 and 100 mm. A comparison between the numerical and measured absorption coefficients of f) the LS, g) the AS, and h) the MLS structures.

varying the size of the openings, as illustrated in **Figure** 9a. We considered different opening sizes, as depicted in the inset of Figure 9a. The measured absorption magnitudes of the LS, MLS, and AS structures, using the standard 100 mm impedance tube, exhibit peaks at 1760, 1560, and 910 Hz, respectively, as shown in Figure 9a. These results align with the first peaks of the respective structures without the PU foam in the 40 mm impedance tube, as depicted in Figure 9b. Furthermore, placing PU foam in front of the proposed structures reveals equivalent absorption performance compared to their respective measurements in the 40 mm impedance tube, as shown in Figure 9c. It's worth noting that melamine foam performs better at low frequencies compared to PU foam due to its higher flow resistivity, as illustrated in Figure 9d. Varying the sizes of the openings has a minor effect on absorption since the performance of a single proposed structure achieves similar results to that of a 100 mm diameter proposed structure with various opening sizes. It's important to note that measurements were only conducted with the porous

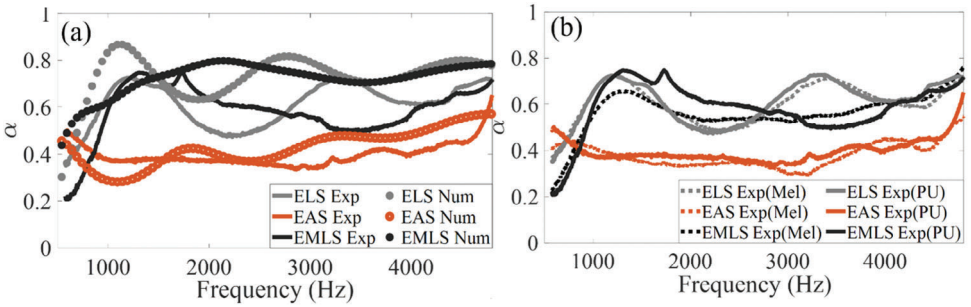

Figure 7. a) A comparison of the numerical and experimental absorption performance of embedded PU foam in the LS, MLS, and AS structures, denoted as ELS, EMLS, and EAS, respectively. b) The measured absorption performance of embedded PU and melamine foam within these same structural configurations.

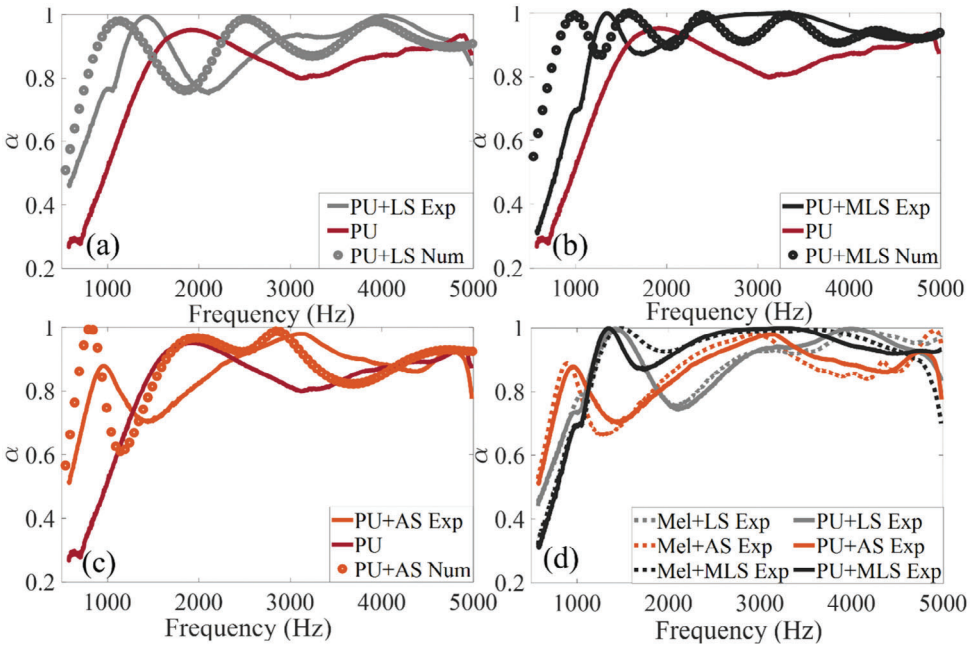

Figure 8. A comparison between the numerical and measured absorption coefficients of a 27 mm thick PU foam when positioned in front of the a) LS, b) MLS, and c) AS structures. d) A comparison of the impact of PU and melamine foam on the measured absorption performances of the proposed structures. The total thickness of the structures with PU foam placed in front of them is 54 mm.

layer placed in front of the proposed structures, as embedding the foam inside the structures proved challenging.

3. Discussion

The uniqueness of the performance of the proposed structures can be described from two perspectives. First, a single unit cell is used to achieve a broadband bandwidth that has comparable performance to state-of-the-art metamaterials that are based on multiple resonators. Based on the causality constraint, that relates the bandwidth and material thickness, a broad bandwidth metamaterial, starting from 800 Hz, has been achieved using multiple resonators with an overall thickness of 60 mm.[28] The MLS structure without PU foam demonstrated approximately similar performance with half the thickness due to the combined effects of Fabry–Pérot resonance and viscous boundary losses along the narrow features of the waveguide. In addition, the gradient inlet reduces reflected waves from the interfaces due to improved impedance matching. Instead of porous foam with a flat rigid backing, replacing it with the proposed structures enhances the low-frequency performance. The other uniqueness is their performance for a broad range of incident angles compared to conventional resonators. The proposed structures possess the merits of low-frequency performance of metamaterials and the high absorption performance of porous materials. Overall, the proposed structures offer a significant leap forward in broadband acoustic metamaterial design. Their ultra-thin and ultra-wide bandwidth properties that cover a wide range of incident angles make them an ideal candidate for room acoustics and for reducing machinery noise.

Since the effective material properties depend on the frequency, achieving a truly frequency-independent absorption using conventional passive materials is almost impossible. This raises the question of how the concept of a frequency-independent antenna can be realized for sound wave absorption. In this regard, delving into the concept of frequency-independent antennas provides a deeper understanding of how such mechanisms can be achieved for sound waves. It remains an open question, as there are no clearly defined values to classify metamaterials into a certain class based on their bandwidth. In electromagnetics, frequency-independent antennas possess an ultra-broadband performance for a wide range of incident angles. In addition, the distinction between broadband antennas and frequency-independent antennas lies in their respective bandwidth (F_U/F_L), where F_U and F_L represent the upper and lower cutoff frequencies. Broadband antennas typically have a bandwidth greater than two, while frequency-independent antennas typically have a bandwidth greater than ten for a wide range of incidence angles. Based on this understanding, the MLS structure and PU-embedded proposed structures share a common characteristic with frequency-independent antennas, in terms of bandwidth and incident angle coverage, achieved using a single unit cell. Particularly, the PU-embedded proposed structures exhibit a bandwidth greater than ten with a single unit cell, in contrast to the use of multiple resonators, while covering wide incident angles. This makes them a different class of sound-absorbing metamaterial, i.e., frequency-independent absorbers, in contrast to commonly used approaches.

4. Conclusion

We have successfully demonstrated a frequency-independent sound absorber by adopting the concept of frequency-independent antennas from radio waves. The proposed approach

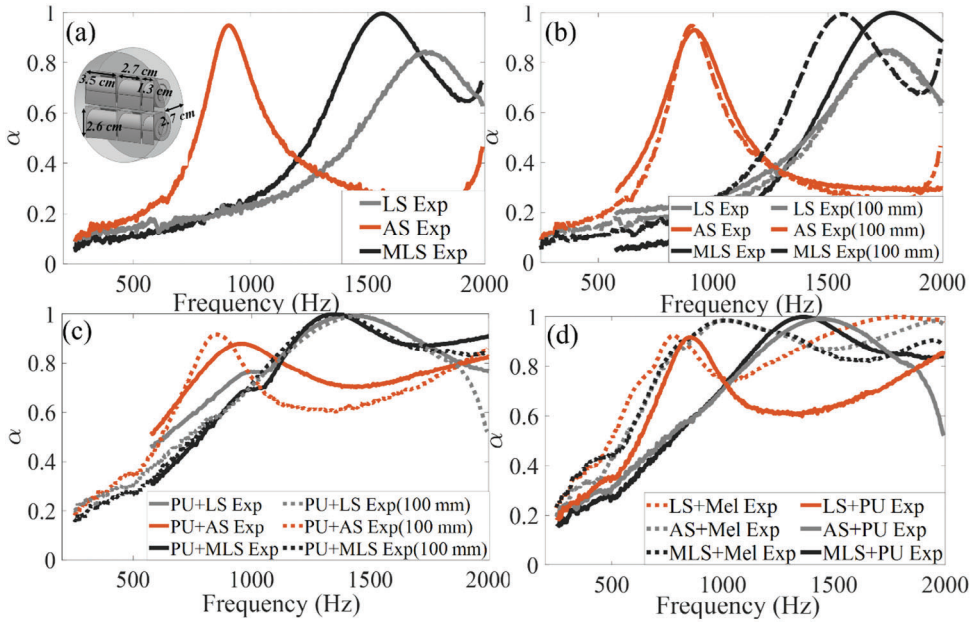

Figure 9. Measured low-frequency absorption coefficients for a) the LS, AS, and MLS structures in a 100 mm impedance tube. The inset illustrates a schematic representation of the LS structure with its opening size. b) A comparison of the measurements in both 100 and 40 mm impedance tubes for the LS, AS, and MLS structures, all without porous foam. c) Comparison of the absorption coefficients when a PU foam is positioned in front of the LS, MLS, and AS structures in both 40 and 100 mm impedance tubes. d) A comparison of the absorption performances of the PU and melamine foams when placed in front of the LS, AS, and MLS structures.

surpasses the performances of the existing state-of-the-art broadband sound-absorbing metamaterials in terms of bandwidth and range of incident angles, demonstrating remarkable similarities to their electromagnetic counterparts. In addition, it opens a pathway to achieve broadband absorption using a single unit cell, without relying on multiple resonators. This remarkable outcome is attributed to the combined effects of Fabry–Pérot resonance, viscous boundary losses arising from the narrow tails of the waveguide, and thermoviscous loss of the foam. Furthermore, the distinction between frequency-independent sound absorbers and conventional metamaterials is clearly defined based on the upper and lower cutoff frequencies, following the case of electromagnetic waves. Notably, the low-frequency performance of the proposed structures has revealed that the size of the opening has less influence on the absorption peak, with the overall absorption performance primarily determined by the total propagation distance of the wave. In general, the compact nature of frequency-independent absorbers allows the integration of metamaterials into practical applications that require broadband frequency and incident angle absorption, such as affordable anechoic chamber construction, room acoustics, and machinery noise reduction.

5. Experimental Section

Numerical Model: Numerical analyses were conducted using the acoustic-thermoviscous pressure domain within the COMSOL Multiphysics software. The absorption characteristics of three structures, namely the Log-Spiral (LS), Modified Log-Spiral (MLS), and Archimedean (AS) structures, were predicted while considering both air and porous materials. 2D simulation were employed to elucidate the working principles of these structures due to the substantial computational resources required for a 3D simulation that takes thermoviscous loss into account. The Poroacoustics module of COMSOL Multiphysics was utilized to predict the absorption performances of the foam embedded within and placed in front of the proposed structures. Polyurethane (PU) foam, characterized by a porosity of 0.95, a tortuosity of 1.42, a viscous characteristic length of 90 μm, a thermal characteristic length of 180 μm, and a flow resistivity of 5500 Pa s m^{-2}, as well as melamine foam, featuring similar porosity and tortuosity to the PU foam, with viscous and thermal characteristic lengths of 180 and 360 μm, and a flow resistivity of 8900 Pa s m^{-2}, were modeled within the porous acoustic domain. To reduce reflections, a perfectly matched layer was utilized, and Floquet boundary conditions were applied in the x and y- directions. The oblique incident angle (θ) was systematically varied from 0° to 89° in 12 equal increments. Furthermore, an additional loss term (γ) was introduced as an imaginary speed of sound, $c \times (1 + \gamma i)$, within the proposed structures, with a dissipation term equal to six percent of the speed of sound in air, accounting for losses during measurements. The total velocity magnitude within the proposed structure was analyzed using the post-processing tools available in COMSOL Multiphysics. In all simulations involving an air medium, a six percent dissipation was chosen based on its close agreement with the first measured absorption peak of the LS structure. The absorption coefficient (α) was calculated as,

$$\alpha = 1 - \left| \frac{Z\cos\theta - Z_0}{Z\cos\theta + Z_0} \right|^2 \tag{2}$$

Measurement Setup: The absorption performances of the samples were measured using standardized two-microphone impedance tubes, as shown in Figure 6a,b, respectively. For low- and high-frequency absorption measurements, 100 and 40 mm impedance tubes were employed with frequency intervals ranging from 250 to 2000 Hz and 550 to 5000 Hz, respectively. Three samples were manufactured for each impedance tube using fused deposition modeling (FDM) and polylactic acid (PLA+), as depicted in Figure 6c,d. Polyurethane and melamine foams were employed,

as shown in Figure 6e. The porous foam was embedded within the proposed structures by printing the samples with an open side, after which the foams were embedded inside. The open sides were subsequently sealed, and Scotch tape was wrapped around the samples to tightly secure them inside the impedance tubes, ensuring a proper fit. To minimize uncertainties during the measurements, four separate measurements were carried out. Melamine and PU foams, each with a thickness of 27 mm and diameters of 40 and 100 mm, were prepared for each standard measurement tube.

Acknowledgements

This project was supported by the Alexander Von Humboldt Foundation.

Conflict of Interest

The authors declare no conflict of interest.

Data Availability Statement

The data that support the findings of this study are available from the corresponding author upon reasonable request.

Keywords

antennas, broad-angle, frequency-independent, metamaterials, sound absorption

Received: July 30, 2023
Revised: October 22, 2023
Published online: December 7, 2023

[1] J. F. Allard, N. Atalla, *Propagation of Sound in Porous Media: Modelling Sound Absorbing Materials*, 2nd ed., John Wiley & Sons, Hoboken, NJ, USA, **2009**.
[2] T. J. Cox, P. D'Antonio, *Acoustic Absorbers and Diffusers: Theory, Design and Application* 2nd ed., Taylor and Francis, Boca Raton, FL, USA **2009**.
[3] V. G. Veselago, *Sov. Phys. Usp.* **1968**, *10*, 509.
[4] J. B. Pendry, A. J. Holden, D. J. Robbins, W. J. Stewart, *IEEE Trans. Microw. Theory Tech.* **1999**, *47*, 2075.
[5] S. A. Cummer, J. Christensen, A. Alù, *Nat. Rev. Mater.* **2016**, *1*, 16001.
[6] Z. Zhang, L. Bai, L. Xu, W. X. Jiang, T. J. Cui, *Phys. Status Solidi (RRL)* **2021**, *15*, 2100163.
[7] A. Song, J. Li, C. Shen, X. Peng, X. Zhu, T. Chen, S. A. Cummer, *Appl. Phys. Lett.* **2019**, *114*, 121902.
[8] Y. Zhu, B. Assouar, *Phys. Rev. B* **2019**, *99*, 174109.
[9] Z. Zhang, W. X. Jiang, X. G. Zhang, W. Cao, C. W. Qiu, T. J. Cui, *Mat. Des.* **2023**, *229*, 111903.
[10] Y. Zhang, H. Cheng, J. Tian, S. Chen, *Phys. Rev. Appl.* **2020**, *14*, 064057.
[11] H. Chen, C. T. Chan, *Appl. Phys. Lett.* **2007**, *91*, 183518.
[12] Z. Liu, X. Zhang, Y. Mao, Y. Y. Zhu, Z. Yang, C. T. Chan, P. Sheng, *Science* **2000**, *289*, 1734.
[13] G. Dolling, C. Enkrich, M. Wegener, C. M. Soukoulis, S. Linden, *Science* **2006**, *312*, 892.
[14] J. Mei, G. Ma, M. Yang, Z. Yang, W. Wen, P. Sheng, *Nat. Commun.* **2012**, *3*, 756.
[15] Y. Li, B. M. Assouar, *Appl. Phys. Lett.* **2016**, *108*, 063502.
[16] N. Jiménez, W. Huang, V. Romero-García, V. Pagneux, J.-P. Groby, *Appl. Phys. Lett.* **2016**, *109*, 121902.
[17] F. Kronowetter, L. Pretsch, Y. K. Chiang, A. Melnikov, S. Sepehrirahnama, S. Oberst, D. A. Powell, S. Marburg, *J. Acoust. Soc. Am.* **2023**, *154*, 842.
[18] N. Gao, Z. Zhang, J. Deng, X. Guo, B. Cheng, H. Hou, *Adv. Mat. Tech.* **2022**, *7*, 2100698.
[19] G. Ma, *P. Sheng, Sci. adv.* **2016**, *2*, 150159.
[20] C. Shao, H. Long, Y. Cheng, X. Liu, *Sci. Rep.* **2019**, *9*, 13482.
[21] Z. Yang, J. Mei, M. Yang, N. H. Chan, P. Sheng, *Phys. Rev. Lett.* **2008**, *101*, 204301.
[22] K. Donda, Y. Zhu, S.-W. Fan, L. Cao, Y. Li, B. Assouar, *Appl. Phys. Lett.* **2019**, *115*, 173506.
[23] X. Cai, Q. Guo, G. Hu, J. Yang, *Appl. Phys. Lett.* **2014**, *105*, 121901.
[24] A. Carvalho de Sousa, E. Deckers, C. Claeys, W. Desmet, *MSSP.* **2021**, *147*, 107102.
[25] G. Catapane, G. Petrone, O. Robin, K. Verdière, *Appl. Acoustics.* **2023**, *209*, 109402.
[26] F. Kronowetter, P. Wagner, J. Kolodi, I. Brabandt, T. Neumeyer, N. Rümmler, S. Marburg, *MSSP.* **2023**, *200*, 110548.
[27] M. Krasikova, S. Krasikov, A. Melnikov, Y. Baloshin, S. Marburg, D. A. Powell, A. Bogdanov, *Adv. Mat. Tech.* **2023**, *8*, 2200711.
[28] M. Yang, S. Chen, C. Fu, P. Sheng, M. Horiz, *Mater. Horiz.* **2017**, *4*, 673.
[29] M. Yang, P. Sheng, *Annu. Rev. Mater. Res.* **2017**, *47*, 83.
[30] Z. Zhou, S. Huang, D. Li, J. Zhu, Y. Li, *Nat. Sci. Rev.* **2022**, *9*, nwab171.
[31] Y. Meng, V. Romero-García, G. Gabard, J.-P. Groby, C. Bricault, S. Goudé, *Adv. Mat. Tech.* **2023**, *8*, 2201909.
[32] S. Qu, P. Sheng, *Phys. Rev. Appl.* **2022**, *17*, 047001.
[33] L. Liu, H. Chang, C. Zhang, X. Hu, *Appl. Phys. Lett.* **2017**, *111*, 083503.
[34] N. Jimenez, O. Umnova, J.-P. Groby, in *Topics is Applied Physics*, (Eds: Y. P. Lee, D. J. Lockwood, P. M. Ossi, K. Yamanouchi), Springer, Berlin **2022**.
[35] Y. Wang, H. Zhao, H. Yang, J. Zhong, J. Wen, *Europhys. Lett.* **2017**, *120*, 54001.
[36] Y. Duan, J. Luo, G. Wang, Z. H. Hang, B. Hou, J. Li, P. Sheng, Y. Lai, *Sci. Rep.* **2015**, *5*, 12139.
[37] J.-P. Groby, O. Dazel, A. Duclos, L. Boeckx, L. Kelders, *J. Acoust. Soc. Am.* **2011**, *130*, 3771.
[38] Y. Zhou, D. Li, Y. Li, T. Hao, *Appl. Phys. Lett.* **2019**, *115*, 093503.
[39] X.-F. Zhu, S.-K. Lau, Z. Lu, W. Jeon, *J. Sound Vib.* **2019**, *461*, 114922.
[40] C. Lagarrigue, J. P. Groby, V. Tournat, O. Dazel, O. Umnova, *J. Acoust. Soc. Am.* **2013**, *134*, 4670.
[41] J.-P. Groby, W. Huang, A. Lardeau, Y. Aurégan, *J. Appl. Phys.* **2015**, *117*, 124903.
[42] J.-P. Groby, C. Lagarrigue, B. Brouard, O. Dazel, V. Tournat, B. Nennig, *J. Acoust. Soc. Am.* **2015**, *137*, 273.
[43] J. Yang, J. S. Lee, Y. Y. Kim, *J. App. Phys.* **2015**, *117*, 174903.
[44] Y. Tang, S. Ren, H. Meng, F. Xin, L. Huang, T. Chen, C. Zhang, T. J. Lu, *Sci. Rep.* **2017**, *7*, 43340.
[45] K. N. Rozanov, *IEEE Trans. Antennas Propag.* **2000**, *48*, 1230.
[46] V. H. Rumsey, in *IRE International Convention Record* **1966**, *5*, 114.
[47] J. D. Kraus, Antennas 2nd ed., TATA McGraw-Hill EDITION, **1988**.
[48] P. E. Mayes, in *Antenna Handbook*, (Eds: Y.T. Lo, S. W. Lee), Springer, Boston, MA, **1988**.
[49] Y. Xie, A. Konneker, B.-I. Popa, S. A. Cummer, *Appl. Phys. Lett.* **2013**, *103*, 201906.
[50] Y. Xie, W. Wang, H. Chen, A. Konneker, B.-I. Popa, S. A. Cummer, *Nat. Commun.* **2014**, *5*, 5553.
[51] https://drive.google.com/file/d/1ZkuDcwvoKIQ36XB28tWFN8kbPyBH7A7m/view?usp=share_link
[52] A. G. Webster, *Proc. Natl. Acad. Sci. USA* **1919**, *5*, 275.
[53] H. Kuttruff, *Acoustics: An Introduction*, 6th ed., Taylor & Francis, Boca Raton, FL, USA **2007**.
[54] S. Wang, B. Hou, C. T. Chan, *Sci. Rep.* **2019**, *9*, 14078.
[55] *Gesellschaft für Akustikforschung Dresden mbH* **2023**, https://www.akustikforschung.de/en/produkte/messgerate/impedanzrohr-acoustitube (February 17).